Dalton Transactions

ROYAL SOCIETY OF CHEMISTRY

PAPER

View Article Online
View Journal | View Issue



Cite this: *Dalton Trans.*, 2026, **55**, 6558

# From cysteines to histidines – chemically distinct Cu(II)-binding motifs in the C-terminal region of archaeal CopT regulators

Wojciech Lizak, [a] Klaudia Kłopotowska,[a] Arian Kola, [b] Daniela Valensin [b,c] and Aleksandra Hecel *[a]

Copper-sensing transcriptional regulators of the CopT family play a central role in archaeal metal homeostasis, enabling adaptation to fluctuating copper availability. Their metal-binding properties have traditionally been rationalized almost exclusively in terms of cysteine-rich TRASH/YHS domains. Here we show that this view is incomplete, demonstrating that short histidine-containing C-terminal motifs outside the TRASH/YHS core possess an intrinsic capacity to form stable and chemically distinct Cu(II)-binding environments. Using minimal peptide models and a combined potentiometric, spectroscopic, and NMR approach, we show that the GHH motif displays a pronounced and persistent thermodynamic preference for both Cu(II) and Zn(II) over the HGH sequence across a broad pH range. Competition simulations demonstrate that this preference is not dictated by histidine spacing alone but correlates with donor-set composition, with glutamate carboxylates enabling early metal anchoring under mildly acidic conditions. Metal binding in both motifs is primarily driven by histidine residues. In the proposed coordination model, the surrounding donor environment is completed by glutamate side chains in the GEEGHH sequence, whereas in the HGH motif methionine occupies this complementary role, residing in close proximity to the Cu(II) coordination sphere and acting as a direct thioether donor in Zn(II) binding. Overall, these results identify histidine- and carboxylate-containing CopT C-terminal motifs as chemically distinct metal-binding elements and demonstrate how differences in donor-set composition encode differential Cu(II) and Zn(II) affinity independently of canonical cysteine-based domains.

Received 27th February 2026,
Accepted 6th April 2026

DOI: 10.1039/d6dt00501b

rsc.li/dalton



## Introduction

Copper-handling pathways in prokaryotes are typically organized as compact, metal-responsive genetic modules that couple intracellular metal sensing with sequestration and active export.[1–4] In bacterial systems, copper stress responses are commonly controlled by dedicated operons encoding P-type ATPases, soluble copper-binding proteins, and metalloregulators whose DNA-binding activity is directly modulated by copper ions.[5–7] Representative examples include Cop-, Cue-, Cus-, and Pco-type systems, in which transcriptional regulation is mediated by metal-sensing repressors or activators belonging to the MerR, ArsR/SmtB, or CsoR families.[8–10] These regulatory modules convert metal coordination events into transcriptional output and rely on well-defined donor sets, most frequently involving histidine, cysteine, and carboxylate residues arranged in short sequence motifs. Such architectures enable rapid adjustment of gene expression to fluctuations in intracellular copper levels while limiting nonspecific metal interactions.[11]

Compared with bacterial models, archaeal copper-resistance systems remain considerably less characterized at the molecular and coordination-chemical level, despite the frequent occurrence of archaea in metal-rich and extreme environments. Genomic analyses of extremophilic archaea reveal conserved gene clusters resembling bacterial *cop* operons, typically comprising a copper-responsive regulator, a copper-binding protein, and a P-type ATPase copper exporter. In *Saccharolobus solfataricus*, the *copTMA* operon encodes CopT, a putative transcriptional regulator, and CopA, an ATPase essential for copper efflux.[12–14] Functional studies demonstrate that copper modulates CopT–DNA interactions, establishing a direct link between metal coordination and transcriptional regulation that parallels, but is mechanistically distinct from, bacterial copper-responsive regulators.[15]

CopT proteins exhibit a bipartite architecture consisting of an N-terminal helix–turn–helix DNA-binding motif and a

[a]*Faculty of Chemistry, University of Wroclaw, 50383 Wroclaw, Poland. E-mail: aleksandra.hecel2@uwr.edu.pl*
[b]*Department of Biotechnology, Chemistry and Pharmacy, University of Siena, 53100 Siena, Italy*
[c]*Consorzio Interuniversitario Risonanze Magnetiche di Metalloproteine (CIRMMP), Via L. Sacconi 6, Sesto Fiorentino 50019, Italy*

C-terminal region classified as a YHS-family domain and functionally described as a TRASH-type metal-binding motif (Trafficking, sensing and heavy-metal binding). TRASH/YHS domains contain conserved cysteine motifs (CXXC and CCXXC) that have been implicated in transition-metal coordination and copper sensing.[16–18] Although copper stress is typically applied experimentally as Cu(II), intracellular copper trafficking and export by CopA-type ATPases are widely associated with Cu(I), suggesting that copper-dependent regulation may be triggered by copper availability, while the chemically bound form in cysteine-rich sites is biased toward Cu(I).[19] From a coordination-chemical perspective, this distinction is significant, as cysteine thiolates preferentially stabilize softer metal ions and lower oxidation states, whereas Cu(II) coordination by thiolates is generally disfavored under oxidizing conditions.[20]

Consistent with this view, available studies on archaeal CopT/CopR regulators primarily provide functional evidence for copper-dependent transcriptional responses and metal-modulated DNA binding, while direct molecular-level characterization of copper coordination within TRASH/YHS domains remains lacking.[12,14,21–23] As a result, copper sensing by CopT-type regulators is commonly interpreted almost exclusively in terms of cysteine-based metal-binding chemistry.

In this context, CopT proteins also contain an additional, chemically distinct feature located within the C-terminal tail region, outside the canonical TRASH/YHS domain. Sequence analyses of CopT homologues from different archaeal species reveal short histidine-containing motifs at their extreme C-termini. In particular, CopT proteins from *Saccharolobus solfataricus* and *Sulfurisphaera tokodaii* terminate with **HGH** and **GHH** motifs, respectively. Although these sequences lie outside the conserved cysteine-rich TRASH core, they are part of the same C-terminal metal-associated region and introduce donor sets dominated by histidine imidazole groups and, in the case of the GHH motif, additional carboxylate side chains. From a coordination-chemical standpoint, such motifs are intrinsically well suited for Cu(II) binding and are fundamentally distinct from cysteine-based copper-binding sites.

Here, we demonstrate that short histidine-containing C-terminal peptide motifs derived from archaeal CopT regulators possess an intrinsic capacity to form stable and well-defined Cu(II) complexes, revealing chemically distinct copper-binding environments within the same C-terminal region. Despite their clear chemical relevance, the metal-binding properties of these motifs have not previously been examined at the molecular level. In particular, it remains unclear whether they merely modulate canonical cysteine-based sites or instead constitute chemically autonomous metal-binding elements with distinct coordination pathways. Although Cu(II) is the biologically relevant metal in copper-responsive systems, Zn(II) was included as a redox-inactive reference ion to evaluate the intrinsic metal-binding preferences of the histidine-containing motifs. Such a comparison allows us to distinguish sequence-encoded donor set effects from metal-specific coordination behavior. Moreover, it has been reported that metal-binding proteins and chaperone-like systems may exhibit a certain degree of metal promiscuity and adjust their coordination preferences depending on metal availability and nutritional conditions.[24–26] Therefore, the inclusion of Zn(II) provides additional context for understanding how these motifs may respond to variations in metal availability.

To address this question, we investigate the Cu(II) and Zn(II) coordination chemistry of two minimal C-terminal peptide motifs derived from CopT proteins from *Saccharolobus solfataricus* (Ac-GPKGMP**HGH**-COOH) and *Sulfurisphaera tokodaii* (Ac-GPKGMPGEE**GHH**-COOH). We combine potentiometric analysis with UV-Vis, circular dichroism, EPR, and NMR spectroscopy to define metal-binding stoichiometry, stability, and donor-set evolution across a broad pH range. This coordination-chemical approach provides molecular-level insight into copper binding by CopT terminal motifs and extends the prevailing cysteine-centered view of copper sensing in archaeal regulators.

## Experimental

### Materials

The peptides (Ac-GPKGMP**HGH**-COOH and Ac-GPKGMPGEE**GHH**-COOH) were purchased from Karebay Biochem (certified purity: 98%) and were used as received. The samples for electrospray ionization mass spectrometry (ESI-MS) were prepared in extra pure methanol (Sigma-Aldrich)–water mixture. Cu(II) and Zn(II) perchlorates were high-purity products [$Cu(ClO_4)_2{\cdot}6H_2O$ from Sigma-Aldrich; $Zn(ClO_4)_2{\cdot}6H_2O$ from POCH]. The concentrations of their stock solutions were determined by inductively coupled plasma mass spectrometry. The 0.1 M NaOH solution (Sigma-Aldrich), which was free of carbonates, was standardized by using potentiometry with potassium hydrogen phthalate (Sigma-Aldrich). All of the samples were prepared with freshly double distilled water. The ionic strength ($I$) was adjusted to 0.1 M by the addition of $NaClO_4$ (Sigma-Aldrich).

### Potentiometric measurements

The stability constants for proton Cu(II) and Zn(II) complexes with two ligands were calculated from titration curves carried out over the pH range of 2–11 at 298 K and ionic strength 0.1 M $NaClO_4$. The total volume of the solution used was 3.0 ml. The potentiometric titrations were performed using a Dosimat 800 Metrohm Titrator connected to a Methrom 905 pH-meter and a Mettler Toledo pH inLab Science electrode. The thermostabilized glass cell was equipped with a magnetic stirring system, a microburet delivery tube and an inlet–outlet tube for argon. Solutions were titrated with 0.1 M carbonate-free NaOH. The electrodes were calibrated daily for hydrogen ion concentration through titrating $HClO_4$ with NaOH using a total volume of 3.0 ml. The ligand concentration was 0.4 mM, and the metal-to-ligand ratios were 0.9 : 1. The exact concentrations and the purities of the ligand solutions were determined by the Gran

method.[27] The standard potential and the slope of the electrode couple were computed by means of GLEE program.[28] The HYPERQUAD 2008 program was used for the stability constant calculation.[29,30] The speciation diagrams were computed with the HYSS program.[31] Hydrolysis constants for metal ions were taken from the literature.[32] A competition plot (competition diagram) is a speciation simulation for a solution containing one metal ion and two (or more) ligands, constructed from independently determined protonation constants of the ligands and stability constants of their metal complexes. The diagram illustrates how the metal ion is distributed between the competing ligands as a function of pH (and concentrations), based entirely on equilibrium constants obtained from potentiometric measurements. The simulation was performed using the HySS program by combining the equilibrium models determined separately for the Cu(II)-peptide systems. Importantly, the calculation is based on binary metal–ligand models, meaning that only species of the type CuL are included in the speciation scheme. Mixed-ligand complexes of the type $CuL_1L_2$ are not considered unless explicitly introduced into the model. Thus, the diagram represents a hypothetical but thermodynamically well-defined situation in which two independent ligands compete for the same metal ion according to their intrinsic stability constants.

### Mass spectrometry

High-resolution mass spectra were obtained on a Bruker compact QTOF (Bruker Daltonik, Bremen, Germany), equipped with electrospray ionization source with an ion funnel. The mass spectrometer was operated in the positive ion mode. The instrumental parameters were as follows: scan range *m*/*z* 100–2000, dry gas – nitrogen, temperature 453 K, and ion energy 5 eV. The capillary voltage was optimized to the highest S/N ratio and it was 4800 V. The samples were prepared in 1 : 1 MeOH : $H_2O$ mixture at pH 7.4 with a M : L molar ratio 0.9 : 1, where $[ligand]_{tot}$ = 0.1 mM. The samples were infused at a flow rate of 3 μL $min^{-1}$. The instrument was calibrated externally with a Tunemix™ mixture (Bruker Daltonik, Germany) in quadratic regression mode. Data were processed by application of the Compass DataAnalysis 4.2 (Bruker Daltonik, Germany) program. The mass accuracy for the calibration was better than 5 ppm, enabling together with the true isotopic pattern (using SigmaFit) an unambiguous confirmation of the elemental composition of the obtained complex.

### Spectroscopic studies

The absorption spectra were recorded on a Jasco-V730 spectrophotometer, in the range 200–800 nm, using a quartz cuvette with an optical path of 1 cm. Circular dichroism spectra were recorded on a Chirascan CD spectrometer in the 200–800 nm range, using a quartz cuvette with an optical path of 1 and 0.1 cm in the visible and near-UV range. The concentration of sample solutions used for spectroscopic studies was similar to those employed in the potentiometric experiment. The metal : ligand ratio was 0.9 : 1. All spectroscopic measurements were recorded in the pH range 3–11. The pH of the samples was adjusted with the appropriate amounts of $HClO_4$ and NaOH solutions. The $\varepsilon$ (UV-Vis) and $\Delta\varepsilon$ (CD) values listed in the tables correspond to the individual complex species identified in the distribution diagrams and were extracted from spectra recorded at the pH values where the respective species is present at its maximum concentration. OrginPro 2016 was used to process and visualize the obtained spectra.

Electron paramagnetic resonance (EPR) spectra were recorded in liquid nitrogen on a Bruker ELEXSYS E500 CW-EPR spectrometer at X-band frequency (frequency = 9.5 GHz, modulation amplitude = 10.00 G) and equipped with an ER 036TM NMR teslameter and an E41 FC frequency counter. Ethylene glycol (25%) was used as a cryoprotectant. Ligand concentration was 1 mM and Cu(II) to ligand ratio = 1 : 1. The EPR parameters were analysed by simulating the experimental spectra using WIN-EPR SIMFONIA software, version 1.2 (Bruker).

### NMR

NMR Structural characterization was performed using a Bruker Avance 600 MHz spectrometer, with data collection carried out at 288 K and 298 K. Samples were prepared by dissolving the peptides (0.5 mM) in a 20 mM phosphate buffer at pH 7.4, supplemented with 10% $D_2O$; sodium 3-(trimethylsilyl)-[2,2,3,3-*d*4]propane sulfonate served as the internal chemical shift reference. Titrations with metal ions were performed using stock solutions of ZnCl and $CuSO_4$. For water signal suppression, the excitation sculpting sequence (2 ms selective pulse) was employed.[33] All spectra were processed through TopSpin 5.0 software, while resonance assignments for protons were achieved by analyzing 2D TOCSY and NOESY experiments.

## Results and discussion

### Potentiometric determination of protonation constants of the CopT C-terminal peptide models

The acid–base equilibria of Ac-GPKGMP**HGH**-COOH and Ac-GPKGMPGEE**GHH**-COOH were determined by potentiometric titrations, and the corresponding cumulative and stepwise constants are collected in in Table 1. In both sequences the N-terminus is acetylated, therefore, protonation equilibria arise exclusively from side-chain and C-terminal functional groups. For Ac-GPKGMP**HGH**-COOH, three protonation sites are detected, giving rise to the species $H_3L$, $H_2L$, and HL. The first deprotonation step ($[H_3L]^{2+} \rightarrow [H_2L]^{+}$; $pK_a$ = 6.25) is assigned to one histidine imidazole group, followed by a second imidazole deprotonation ($[H_2L]^{+} \rightarrow [HL]$; $pK_a$ = 7.19). The final deprotonation step within the studied range corresponds to the lysine side-chain ammonium group ($[HL] \rightarrow [L]^{-}$; $pK_a$ = 10.34) (Table 1(A)).

The peptide Ac-GPKGMPGEE**GHH**-COOH displays a more complex acid–base pattern, with six protonation sites (Table 1 (B)). The first three deprotonation steps ($[H_6L]^{3+} \rightarrow [H_5L]^{2+}$,

 

**Table 1** Deprotonation constants ($pK_a$) for (A) Ac-GPKGMP**HGH**-COOH and (B) Ac-GPKGMPGEE**GHH**-COOH peptides at $T$ = 298 K and $I$ = 0.1 M ($NaClO_4$). Values in parentheses are standard deviations on the last significant figure

| Species | $\log\beta$ | $\log K$ | aa |
|---|---|---|---|
| (A) Ac-GPKGMP**HGH**-COOH | | | |
| $[H_3L]^{2+}$ | 23.78(3) | 6.25 | $-N_{im}$ (His) |
| $[H_2L]^{+}$ | 17.53(2) | 7.19 | $-N_{im}$ (His) |
| [HL] | 10.34(1) | 10.34 | $-\varepsilon NH_2$ (Lys) |
| (B) Ac-GPKGMPGEE**GHH**-COOH | | | |
| $[H_6L]^{3+}$ | 35.38(7) | 2.51 | $-COO^-$ (C-term) |
| $[H_5L]^{2+}$ | 32.87(5) | 3.91 | $-COO^-$ (Glu) |
| $[H_4L]^{+}$ | 28.96(5) | 4.74 | $-COO^-$ (Glu) |
| $[H_3L]$ | 24.22(4) | 6.75 | $-N_{im}$ (His) |
| $[H_2L]^{-}$ | 17.47(3) | 7.53 | $-N_{im}$ (His) |
| $[HL]^{2-}$ | 9.94(2) | 9.94 | $-\varepsilon NH_2$ (Lys) |

$[H_5L]^{2+} \rightarrow [H_4L]^{+}$, $[H_4L]^{+} \rightarrow [H_3L]$; $pK_a$ = 2.51, 3.91, and 4.74) are assigned to carboxylic groups originating from the C-terminal carboxyl group and two glutamate side chains. The next two steps ($[H_3L] \rightarrow [H_2L]^{-}$ and $[H_2L]^{-} \rightarrow [HL]^{2-}$; $pK_a$ = 6.75 and 7.53) correspond to deprotonation of the two histidine imidazole groups. The difference between these values suggests nonequivalent local environments of the histidine residues within the sequence. The final deprotonation step ($[HL]^{2-} \rightarrow [L]^{3-}$; $pK_a$ = 9.94) is attributed to the lysine side-chain ammonium group.[34]

It is worth noting that the $pK_a$ value of the C-terminal carboxyl group for Ac-GPKGMP**HGH**-COOH could not be determined, as its deprotonation occurs below the lower limit of the experimental pH range. In contrast, for Ac-GPKGMPGEE**GHH**-COOH, the presence of glutamate side chains shifts the deprotonation of the C-terminal carboxyl group into the measurable pH range, allowing it to be resolved in the fitted equilibrium model.[35–37]

### ESI-MS analysis of Cu(II) and Zn(II) peptide complexes

Electrospray ionization mass spectrometry (ESI-MS) was employed to verify the purity of the investigated ligands and to establish the stoichiometry of their complexes with Cu(II) and Zn(II) ions. In all cases, the spectra confirm formation of predominantly mononuclear metal–peptide species, while no signals attributable to bis-ligand or polynuclear complexes were detected under the applied experimental conditions (Tables S1–S2 and Fig. S1–S2).

For Ac-GPKGMP**HGH**-COOH, the spectra recorded in the presence of Cu(II) show a set of signals corresponding to the free ligand observed in multiple charge states, including $m/z$ 959.41 ($[L]^{+}$), 480.21 ($[L]^{2+}$), and 320.47 ($[L]^{3+}$). In addition to the protonated peptide ions, typical alkali metal adducts such as $[L + Na]^{+}$ and $[L + K]^{+}$ are also detected. The 1 : 1 metal-to-ligand stoichiometry is supported by the signal at $m/z$ 510.17, assigned to the $[CuL]^{2+}$ ion (Table S1(A) and Fig. S1A). For Ac-GPKGMPGEE**GHH**-COOH, the ESI-MS spectrum shows a complete series of ions corresponding to the free ligand, its alkali metal adducts, and copper-bound species across charge states $z$ = 1–3. The protonated peptide is observed at $m/z$ 1274.50 ($[L]^{+}$) and 637.75 ($[L]^{2+}$). A consistent sodium adduct series accompanies the free ligand, including $[L + Na]^{+}$ ($m/z$ 1296.48), $[L + 2Na]^{+}$ ($m/z$ 1318.46), $[L + Na]^{2+}$ ($m/z$ 648.74), and $[L + 2Na]^{2+}$ ($m/z$ 659.73), as well as triply charged species detected at lower $m/z$, such as $[L + Na]^{3+}$ ($m/z$ 432.83), $[L + 2Na]^{3+}$ ($m/z$ 440.16), and $[L + 3Na]^{3+}$ ($m/z$ 447.48). The 1 : 1 complex is detected at $m/z$ 1335.41 ($[CuL]^{+}$), 668.21 ($[CuL]^{2+}$), and 445.80 ($[CuL]^{3+}$). Corresponding sodium adducts of the complex are also present for each charge state, including $[CuL + Na]^{+}$ ($m/z$ 1357.39), $[CuL + Na]^{2+}$ ($m/z$ 679.20), $[CuL + Na]^{3+}$ ($m/z$ 453.13) and $[CuL + 2Na]^{3+}$ ($m/z$ 460.45) (Table S1(B) and Fig. S1B).

In the case of zinc(II) complexes the ESI-MS spectra show an analogous pattern to that observed for copper(II), confirming the formation of exclusively mononuclear Zn(II)-peptide species under the applied experimental conditions (Table S2 and Fig. S2). For Ac-GPKGMP**HGH**-COOH, the spectrum recorded in the presence of Zn(II) contains a series of ions corresponding to the free ligand and its alkali metal adducts, including $[L]^{+}$ at $m/z$ 959.46, $[L + Na]^{+}$ at $m/z$ 981.45, and $[L + K]^{+}$ at $m/z$ 997.41. Doubly charged ions of the ligand are also observed at $m/z$ 480.24 ($[L]^{2+}$), together with $[L + Na]^{2+}$ ($m/z$ 491.23), $[L + K]^{2+}$ ($m/z$ 499.21), and $[L + 2Na]^{2+}$ ($m/z$ 502.22). The 1 : 1 metal-to-ligand stoichiometry is clearly supported by the signal at $m/z$ 510.20, assigned to the $[ZnL]^{2+}$ ion. Additional peaks at $m/z$ 521.20 and 529.19 correspond to the sodium and potassium adducts of the complex, $[ZnL + Na]^{2+}$ and $[ZnL + K]^{2+}$, respectively (Table S2(A) and Fig. S2A). For Ac-GPKGMPGEE**GHH**-COOH, the spectrum similarly shows the presence of doubly charged ions of the free ligand and its alkali metal adducts, with $[L]^{2+}$ observed at $m/z$ 637.79, $[L + Na]^{2+}$ at $m/z$ 648.78, $[L + K]^{2+}$ at $m/z$ 656.77, and $[L + 2Na]^{2+}$ at $m/z$ 659.77. The formation of the zinc complex is evidenced by the signal at $m/z$ 668.75, assigned to $[ZnL]^{2+}$. The corresponding sodium adduct of the complex, $[ZnL + Na]^{2+}$, is detected at $m/z$ 679.74 (Table S2(B) and Fig. S2B).

### Potentiometric and spectroscopic studies of Cu(II) complexes

The Cu(II) coordination properties of the Ac-GPKGMP**HGH**-COOH and Ac-GPKGMPGEE**GHH**-COOH peptides were characterized using a combined potentiometric and spectroscopic approach. Stability constants together with UV-Vis, CD and EPR parameters enabled consistent assignment of the donor sets present in the individual complex species (Table 2).

For the Ac-GPKGMP**HGH**-COOH peptide, the first calculated species is $[CuHL]^{2+}$, which dominates at pH 5.5 (Table 2 (A) and Fig. 1A), indicating the involvement of two imidazole nitrogen atoms from histidine residues already at this pH. The coordination of two nitrogen donor atoms is supported by the d–d absorption band at 655 nm ($\varepsilon$ = 54 $M^{-1}$ $cm^{-1}$) (Table 2(A) and Fig. 1B) and by EPR parameters ($A_{II}$ = 161 G, $g_{II}$ = 2.30) (Table 2(A) and Fig. 1D). Additionally, the presence of a charge-transfer band in the CD spectrum at 234 nm ($\Delta\varepsilon$ = −1.87 $M^{-1}$ $cm^{-1}$) (Table 2(A) and Fig. 1C) is consistent with a ligand-to-metal charge transfer transition from imidazole groups to Cu(II), further supporting the participation of histidine residues in the coordination sphere. The next species, $[CuH_{-1}L]$, reaches its maximum concentration at approxi-

**Table 2** Equilibrium constants, spectroscopic parameters and proposed coordination modes for (A) Cu(II)–Ac-GPKGMP**HGH**-COOH and (B) Cu(II)–Ac-GPKGMPGEE**GHH**-COOH at $T$ = 298 K and $I$ = 0.1 M ($NaClO_4$). M : L ratio was 1 : 1. Values in parentheses are standard deviations on the last significant figure

| | | | UV–Vis | | CD | | EPR | |
|---|---|---|---|---|---|---|---|---|
| Species | $\log \beta_{ijk}$ [a] | $pK_a$ [b] | $\lambda$ [nm] | $\varepsilon$ [$M^{-1}$ $cm^{-1}$] | $\lambda$ [nm] | $\Delta\varepsilon$ [$M^{-1}$ $cm^{-1}$] | $A_{II}$ [G] | $g_{II}$ |
| (A) Cu(II)–Ac-GPKGMP**HGH**-COOH | | | | | | | | |
| $[CuHL]^{2+}$ | 17.39(2) | | 659 | 35.5 | 234 | −1.87 | 161 | 2.30 |
| $[CuH_{-1}L]$ | 3.80(3) | | 337 | 580.9 | 235 | −6.52 | 180 | 2.24 |
| | | | 578 | 104.5 | 302 | −1.26 | | |
| | | | | | 347 | 1.85 | | |
| | | | | | 585 | 0.77 | | |
| $[CuH_{-2}L]^{-}$ | −6.08(4) | 9.88 | 333 | 598.9 | 232 | −1.70 | 184 | 2.20 |
| | | | 570 | 115.3 | 293 | −0.94 | | |
| | | | | | 341 | 1.38 | | |
| | | | | | 478 | −0.37 | | |
| | | | | | 593 | 0.75 | | |
| $[CuH_{-3}L]^{2-}$ | −16.71(4) | 10.63 | 333 | 473.9 | 234 | 2.87 | | |
| | | | 569 | 115.1 | 288 | −0.60 | | |
| | | | | | 329 | 1.50 | | |
| | | | | | 485 | −0.60 | | |
| | | | | | 607 | 0.90 | | |
| (B) Cu(II)–Ac-GPKGMPGEE**GHH**-COOH | | | | | | | | |
| $[CuH_3L]^{2+}$ | 29.16(4) | | | | 228 | −3.81 | 121 | 2.41 |
| $[CuH_2L]^{+}$ | 24.71(1) | 4.45 | 252 | 379.2 | 228 | −4.08 | | |
| | | | 753 | 8.9 | 255 | 0.86 | | |
| $[CuHL]$ | 20.03(2) | 4.68 | 251 | 886.5 | 223 | −6.80 | 144 | 2.30 |
| | | | 667 | 15.9 | 252 | 2.70 | | |
| $[CuL]^{-}$ | 14.81(2) | 5.22 | 252 | 1222.4 | 225 | −8.20 | 142 | 2.30 |
| | | | 649 | 20.0 | 253 | 3.78 | | |
| $[CuH_{-1}L]^{2-}$ | 6.81(3) | 8.00 | 254 | 1444.0 | 227 | −3.37 | 147 | 2.30 |
| | | | 619 | 29.6 | 251 | 2.95 | | |
| | | | | | 345 | 0.35 | | |
| $[CuH_{-2}L]^{3-}$ | −1.18(2) | 7.99 | 257 | 1655.5 | 251 | 2.98 | 174 | 2.23 |
| | | | 581 | 39.3 | 302 | −0.25 | | |
| | | | | | 337 | 0.47 | | |
| $[CuH_{-3}L]^{4-}$ | −10.18(3) | 9.00 | 260 | 1723.9 | 258 | 2.91 | 197 | 2.19 |
| | | | 525 | 54.0 | 305 | −0.75 | | |
| | | | | | 560 | −0.19 | | |
| | | | | | 662 | 0.43 | | |

[a] Cu(II) stability constants are presented as cumulative $\log \beta_{ijk}$ values. L stands for a fully deprotonated peptide ligand that binds Cu(II) ions: $\beta(M_iH_jL_k) = [M_iH_jL_k]/([M]^i[H]^j[L]^k)$, where [L] is the concentration of the fully deprotonated peptide. [b] $pK_a$ values of the peptides were derived from cumulative constants: $pK_a = \log \beta(H_jL_k) - \log \beta(H_{j-1}L_k)$. For Cu(II) complexes: $pK_a = \log \beta(M_iH_j + 1L_k) - \log \beta(M_iH_jL_k)$.

mately pH 8 (Table 2(A) and Fig. 1A) and results from the deprotonation of two additional amide nitrogen atoms. These two amide groups appear to deprotonate within a very narrow pH range; therefore, the intermediate $[CuL]^{+}$ species could not be resolved in the calculations. The involvement of amide donors is supported by CD bands at 302 and 347 nm ($\Delta\varepsilon$ = −1.26, 1.85 $M^{-1}$ $cm^{-1}$), assigned to ligand-to-metal charge-transfer transitions from deprotonated amide nitrogen atoms to Cu(II) (Table 2(A) and Fig. 1C). Coordination by three nitrogen donors is further indicated by the d–d transition band at 569 nm ($\varepsilon$ = 178.2 $M^{-1}$ $cm^{-1}$) (Table 2(A) and Fig. 1B) and EPR parameters ($A_{II}$ = 180 G, $g_{II}$ = 2.24), consistent with a $1N_{im}$, $2N^{-}$ donor set (Table 2(A) and Fig. 1D). The involvement of a third amide nitrogen donor is observed for the $[CuH_{-2}L]^{-}$ species, which reaches its maximum concentration at approximately pH 10 (Table 2(A) and Fig. 1A). For this complex, a $1N_{im}$, $3N^{-}$ coordination mode is proposed. The participation of four nitrogen donors is supported by EPR spectroscopy ($A_{II}$ = 184 G, $g_{II}$ = 2.20) (Table 2(A) and Fig. 1D). The positive ($\lambda$ = 593 nm, $\Delta\varepsilon$ = 0.75 $M^{-1}$ $cm^{-1}$) and negative ($\lambda$ = 478 nm, $\Delta\varepsilon$ = −0.37 $M^{-1}$ $cm^{-1}$) Cotton effects observed in the CD spectrum are consistent with a square-planar geometry of the complex (Table 2(A) and Fig. 1C). The final species, $[CuH_{-3}L]^{2-}$, predominates above pH 11 and results from the deprotonation of a non-coordinated lysine side chain, whose $pK_a$ is comparable to that of the free ligand ($pK_a$ 10.63) (Table 2(A)). The absence of significant changes in the CD and UV-Vis spectra indicates that the binding mode remains unchanged, corresponding to the same $1N_{im}$, $3N^{-}$ coordination as in the preceding species.

Potentiometric measurements revealed that Cu(II) begins to form complexes with the Ac-GPKGMPGEE**GHH**-COOH peptide above pH 3 (Table 2(B) and Fig. 2A) initially forming the $[CuH_3L]^{2+}$ species, in which the metal ion is most likely coordinated by deprotonated glutamate side-chain carboxylate groups. Although three acidic groups (two Glu side chains and the C-terminus) are deprotonated in this species, the available data do not allow us to unambiguously determine how many of them are directly involved in Cu(II) coordination, and a

 

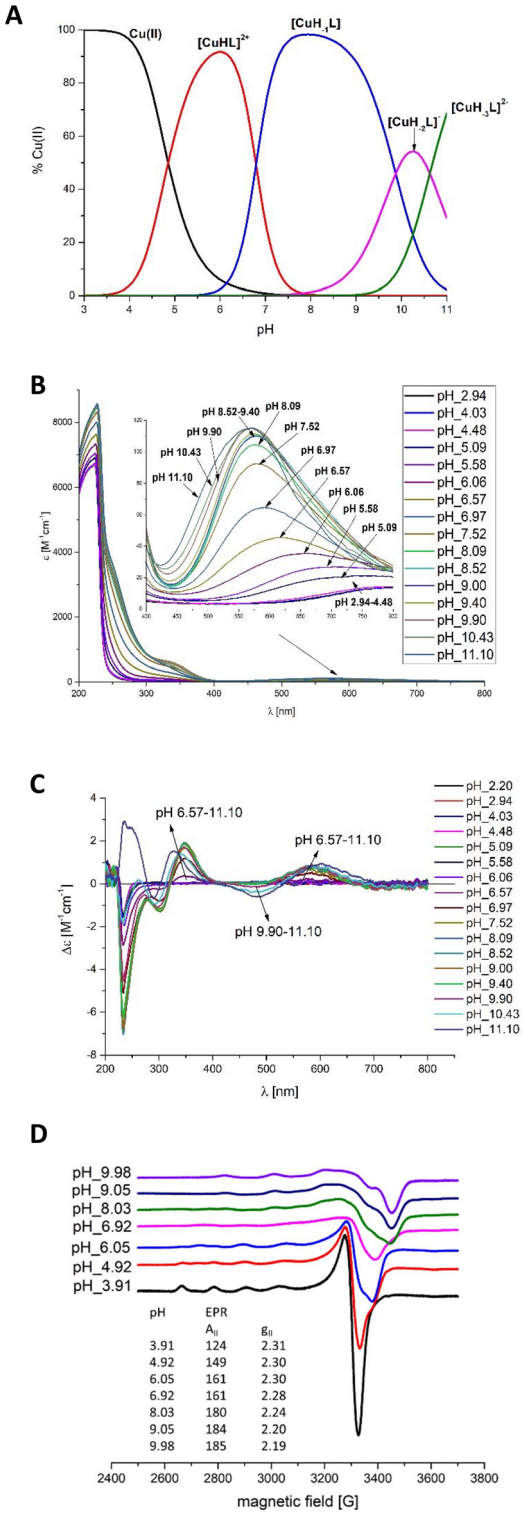


**Fig. 1** (A) Distribution diagrams, (B) pH-dependent UV-Vis absorption spectra, (C) pH-dependent CD spectra, (D) X-band EPR spectra of frozen solution (77 K) at different pH values for Cu(II)–Ac-GPKGMPHGH-COOH in aqueous solution of 4 mM $HClO_4$ with $I$ = 0.1 M $NaClO_4$, $T$ = 298 K, M : L molar ratio = 0.9 : 1.

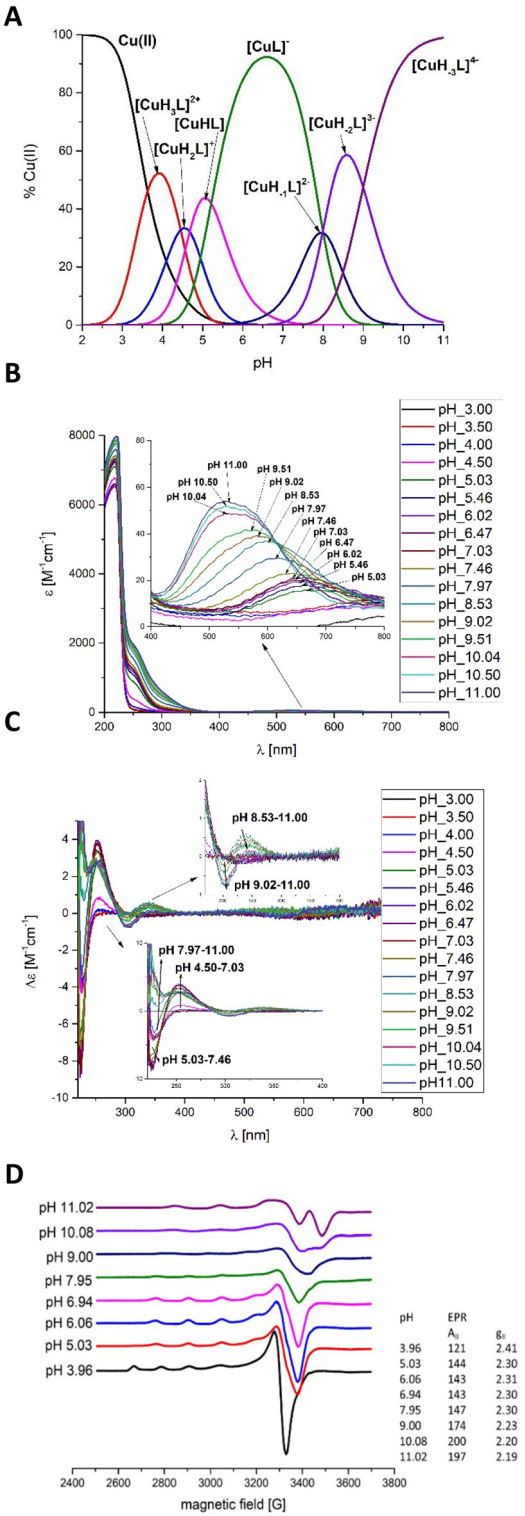


**Fig. 2** (A) Distribution diagrams, (B) pH-dependent UV-Vis absorption spectra, (C) pH-dependent CD spectra, (D) X-band EPR spectra of frozen solution (77 K) at different pH values for Cu(II)–Ac-GPKGMPGEEGHH-COOH in aqueous solution of 4 mM $HClO_4$ with $I$ = 0.1 M $NaClO_4$, $T$ = 298 K, M : L molar ratio = 0.9 : 1.

dynamic exchange between alternative carboxylate coordination modes cannot be excluded. In addition, no spectroscopic features indicative of nitrogen donor coordination are observed in the pH range where $[CuH_3L]^{2+}$ reaches its maximum concentration, supporting the predominance of oxygen donor coordination. The $[CuH_2L]^{+}$ species reaches its maximum concentration at pH 4.5, with Cu(II) coordinated by one imidazole nitrogen atom from a histidine residue (Table 2 (B) and Fig. 2A). A significant decrease in the p$K_a$ value of the complex (4.45) relative to the free ligand (6.75) supports the coordination of Cu(II) by the first histidine residue (Table 2 (B)). The involvement of a single nitrogen donor is supported by the d–d absorption band at 753 nm (Table 2(B) and Fig. 2B) and by two LMCT (Ligand to Metal Charge Transfer) bands observed in the CD spectrum in the 220–250 nm range, assigned to ligand-to-metal charge-transfer transitions from imidazole nitrogen donors to Cu(II), consistent with the participation of the histidine side chain in the coordination sphere (Table 2(B) and Fig. 2C). With increasing pH, the [CuHL] species appears, involving coordination of a second imidazole nitrogen donor (Table 2(B) and Fig. 2A). The blue shift observed in the UV-Vis spectrum (753 → 667 nm) indicates the engagement of a second histidine residue in the coordination sphere (Table 2(B) and Fig. 2B). The EPR parameters ($A_{II}$ = 144 G, $g_{II}$ = 2.30) are also consistent with a 2N binding mode (Table 2(B) and Fig. 2D). Furthermore, the increased intensity of the CD bands in the 220–250 nm range supports the involvement of a second imidazole group in Cu(II) coordination (Table 2(B) and Fig. 2C). The $[CuL]^{-}$ species reaches its maximum concentration at approximately pH 6.5 (Fig. 2A) and does not exhibit significant changes in the UV-Vis, CD, or EPR spectra compared to the [CuHL] complex, indicating that the coordination mode remains unchanged (Table 2(B) and Fig. 2B–D). In particular, no new bands appear in the CD spectrum in the region characteristic of amide nitrogen charge-transfer transitions, which excludes amide donors from participation in the coordination sphere at this stage. However, the p$K_a$ value of 5.22 determined for this species suggests the involvement of a late-deprotonating acidic side chain, most likely a glutamic acid residue, possibly in a stabilizing role. Similar p$K_a$ values (~5) have been reported previously and were attributed to the participation of carboxylate groups in metal binding.[38,39] The observed p$K_a$ is too low to be assigned to the deprotonation of a coordinated water molecule.[40–42] This behavior may also be associated with a dynamic coordination environment, where carboxylate groups, although deprotonated at lower pH, may participate more effectively in metal binding at higher pH as a result of ligand exchange and redistribution processes. The $[CuH_{-1}L]^{2-}$ species, predominant at pH 8, corresponds to coordination involving the first amide nitrogen donor (Table 2(B) and Fig. 2A). A characteristic LMCT band at 345 nm ($\Delta\varepsilon$ = 0.35 $M^{-1}$ $cm^{-1}$) appears in the CD spectrum (Table 2(B) and Fig. 2C), while the d–d band at 619 nm in the UV-Vis spectrum is consistent with a $2N_{im}$, $1N^{-}$ coordination mode. The $[CuH_{-2}L]^{3-}$ species (pH max 8.6) (Table 2(B) and Fig. 2A) involves coordination of a second amide nitrogen donor, indicated by two LMCT bands at 302 nm ($\Delta\varepsilon$ = −0.25 $M^{-1}$ $cm^{-1}$) and 337 nm ($\Delta\varepsilon$ = 0.47 $M^{-1}$ $cm^{-1}$) in the CD spectrum (Table 2(B) and Fig. 2C). Concurrently, one histidine donor is replaced, while the complex maintains a 3N donor set, consistent with the UV-Vis d–d band position ($\lambda$ = 581 nm, $\varepsilon$ = 39.3 $M^{-1}$ $cm^{-1}$) and EPR parameters ($A_{II}$ = 174 G, $g_{II}$ = 2.23) (Table 2(B) and Fig. 2B, D). Finally, the $[CuH_{-3}L]^{4-}$ species corresponds to a $1N_{im}$, $3N^{-}$ coordination mode (Table 2(B) and Fig. 2A). The participation of four nitrogen donors is supported by a blue shift of the d–d band to 525 nm (Table 2(B) and Fig. 2B) and by the EPR parameters ($A_{II}$ = 197 G, $g_{II}$ = 2.19) (Table 2(B) and Fig. 2D). The CD spectrum shows a positive Cotton effect at 662 nm ($\Delta\varepsilon$ = 0.43 $M^{-1}$ $cm^{-1}$) and a negative Cotton effect at 560 nm ($\Delta\varepsilon$ = −0.19 $M^{-1}$ $cm^{-1}$), consistent with a square-planar geometry of the complex (Table 2(B) and Fig. 2C).

### NMR spectroscopic insight into Cu(II) coordination in the C-terminal HGH and GHH motifs

To gain residue-specific insight into the Cu(II) coordination modes inferred from potentiometric and spectroscopic studies, NMR experiments were performed for both C-terminal CopT peptide models containing the **HGH** and **GHH** motifs. Owing to the strong paramagnetic relaxation enhancement induced by Cu(II), sub-stoichiometric metal additions were employed to preserve sufficient spectral resolution and to allow identification of residues located in close spatial proximity to the metal center. NMR experiments were performed at pH 7.4 to probe the metal–peptide interactions under near-physiological conditions and to identify the donor groups involved in metal binding in a biologically relevant environment.

Comparison of the NMR spectra of the apo Ac-GPKGMP**HGH**-COOH peptide with those recorded upon Cu(II) addition revealed pronounced paramagnetic effects localized in the C-terminal region. Even at sub-stoichiometric Cu(II) concentrations, a complete disappearance of the amide and aromatic correlations associated with His7 and His9 was observed (Fig. 3A), together with the loss of their Hα–Hβ cross-peaks (Fig. 3B). In addition to the histidine residues, selective perturbations were detected for Met5. The NH-Hβ correlation of Met5 vanished completely, while the NH-Hα correlation exhibited pronounced line broadening, whereas the remaining aliphatic correlations of this residue remained largely unaffected. This pattern indicates a specific spatial orientation of Met5 relative to the Cu(II) coordination sphere rather than direct metal binding. Furthermore, significant line broadening was observed for correlations involving the Hα proton of Pro6, suggesting its close proximity to the metal center. Notably, the presence of proline immediately preceding the HGH motif precludes backbone amide coordination at this position, consistent with the delayed involvement of amide nitrogens inferred from potentiometric speciation.

For the Ac-GPKGMPGEE**GHH**-COOH peptide, monitoring the titration by 1D NMR revealed an immediate and pronounced line broadening of the Hε1 and Hδ2 aromatic

 

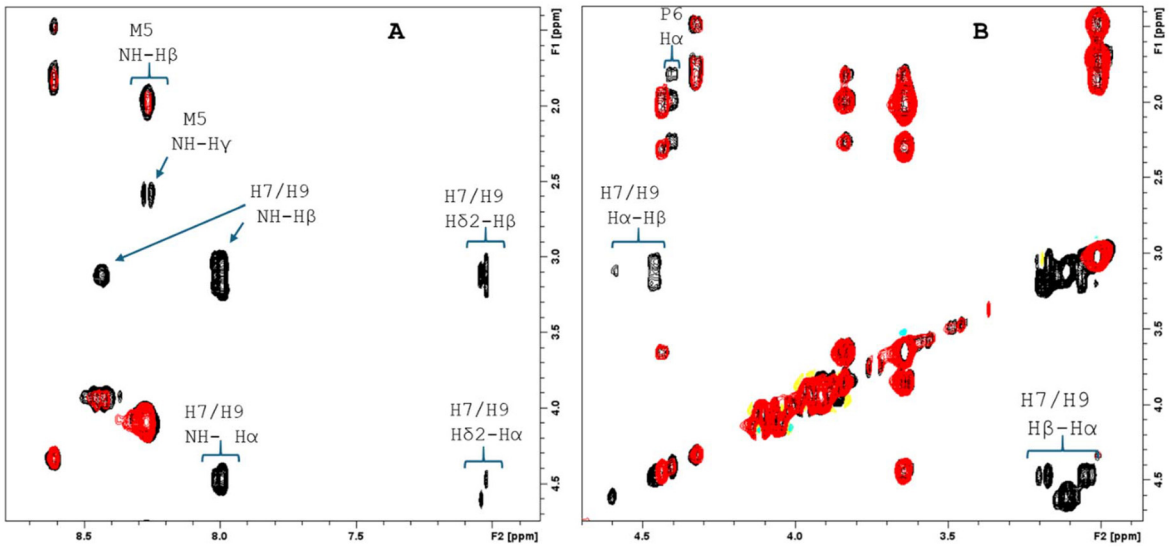


**Fig. 3** Superimposition of the amide and aromatic (A) and aliphatic (B) regions of 2D $^{1}$H–$^{1}$H TOCSY spectra of Ac-GPKGMP**HGH**-COOH recorded in absence (black) and in presence of 0.05 Cu(II) eq. (blue). $T$ = 288 K, $C_M$ = 0.5 mM, phosphate buffer = 20 mM, pH 7.4.

protons of both His11 and His12 upon addition of as little as 0.01 equivalents of Cu(II), followed by their near-complete disappearance at 0.03 equivalents (Fig. 4). This behavior unambiguously identifies the two adjacent histidine residues as the primary Cu(II) anchoring sites. Further information was obtained from 2D TOCSY spectra. A complete broadening of the Hα–Hδ and Hα–Hβ correlations was observed for Pro6, while the corresponding correlations of Pro2 remained largely unaffected, indicating a specific spatial proximity of Pro6 to the metal-binding region. In addition, the simultaneous disappearance of the Hα–Hγ correlations for both Glu8 and Glu9 suggests the involvement of at least one glutamate side chain in Cu(II) coordination (Fig. 5). The equivalently affected signals of both glutamate residues are consistent with a dynamic binding scenario in which the Cu(II) ion undergoes rapid exchange between the two carboxylate groups. These NMR observations provide strong, site-specific evidence that Cu(II) coordination in the GHH peptide involves both histidine residues and at least one glutamate side chain, forming a compact and stabilized binding pocket in the C-terminal region. This

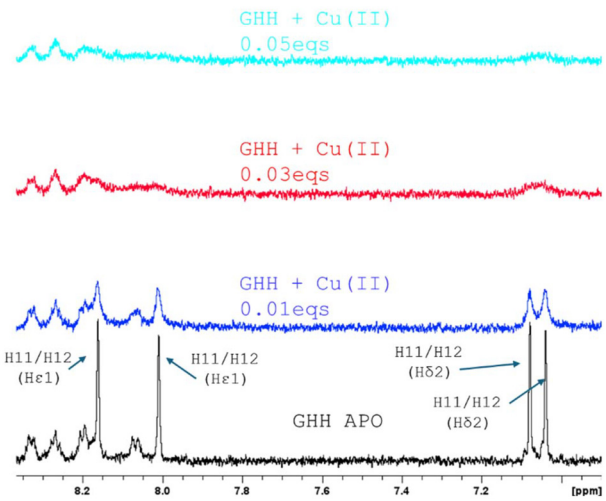


**Fig. 4** Superimposition of the 1D spectra of Ac-GPKGMPGEE**GHH**-COOH recorded in absence (black), in presence of 0.01 Cu(II) eq. (blue), 0.03 Cu(II) eq. (red) and 0.05 Cu(II) eq. (cyan). $T$ = 288 K, $C_M$ = 0.5 mM, phosphate buffer = 20 mM, pH 7.4.

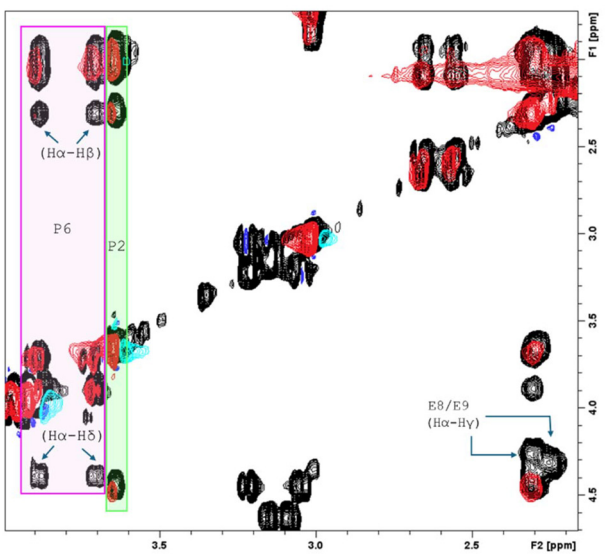


**Fig. 5** Superimposition of the aliphatic regions of 2D $^{1}$H–$^{1}$H TOCSY spectra of Ac-GPKGMPGEE**GHH**-COOH recorded in absence (black) and in presence of 0.05 Cu(II) eq. (red). $T$ = 288 K, $C_M$ = 0.5 mM, phosphate buffer = 20 mM, pH 7.4.

finding directly supports the potentiometric model, in which early Cu(II) anchoring *via* carboxylate donors precedes histidine coordination and facilitates subsequent formation of more stable nitrogen-rich species.

Overall, the NMR experiments performed at pH 7.4 probe the Cu(II)–peptide systems under conditions where well-defined dominant complex species are present according to the potentiometric speciation models. The residue-specific paramagnetic effects observed by NMR are fully consistent with the coordination modes inferred from UV-Vis, CD, and EPR spectroscopy, confirming histidine-based anchoring for both motifs and additional carboxylate involvement in the GHH sequence. Thus, NMR provides independent, site-resolved validation of the Cu(II) binding modes that are thermodynamically relevant at near-physiological pH.

The residue-specific paramagnetic effects observed by NMR at pH 7.4, together with the dominant species identified by potentiometric speciation and supported by UV–Vis, CD and EPR spectroscopy, provide a consistent experimental basis for an integrative representation of Cu(II) binding in the HGH (Fig. 6A) and GHH (Fig. 6B) C-terminal motifs. The schematic models shown in Fig. 6 are intended to summarize how the experimentally established donor sets are organized within the C-terminal regions and to emphasize sequence-dependent differences between the HGH and GHH motifs.

### Cu(II) *vs.* HGH *vs.* GHH

The competition plot reveals a pronounced and highly differential preference of Cu(II) for the **GHH** motif over the **HGH** across the entire pH range (Fig. 7). This behavior originates from fundamental differences in the coordination pathways available to the two sequences. In the **GEEGHH**-derived motif, the presence of glutamate carboxylate groups enables early anchoring of Cu(II) at mildly acidic pH, prior to histidine deprotonation. This initial interaction facilitates subsequent involvement of imidazole nitrogen donors and promotes a smooth transition toward amide nitrogen coordination as the pH increases. In contrast, the HGH sequence lacks acidic side chains and can engage Cu(II) only after histidine deprotonation, resulting in delayed and less effective complex formation.

Importantly, this result should not be interpreted as evidence that adjacent histidines (HH) are generally stronger Cu(II)-binding motifs than separated histidines (HXH). The literature on Cu(II)-histidine peptides shows that the relationship between histidine spacing and complex stability is not universal. Some studies explicitly report cases where HH motifs constitute preferred Cu(II) binding sites,[43–46] whereas others demonstrate that motifs with separated histidines (HXH, HXXH) can be equally effective or even favored, particularly when the peptide backbone geometry facilitates the formation of amide-rich $1N_{im}$, $3N^{-}$ coordination modes at higher pH.[47–51] In Cu(II) complexes, these amide-involving species are often the dominant thermodynamic contributors to overall stability, which diminishes the predictive value of imidazole proximity alone. A further difference is the presence of a proline residue directly adjacent to the HGH binding site. The

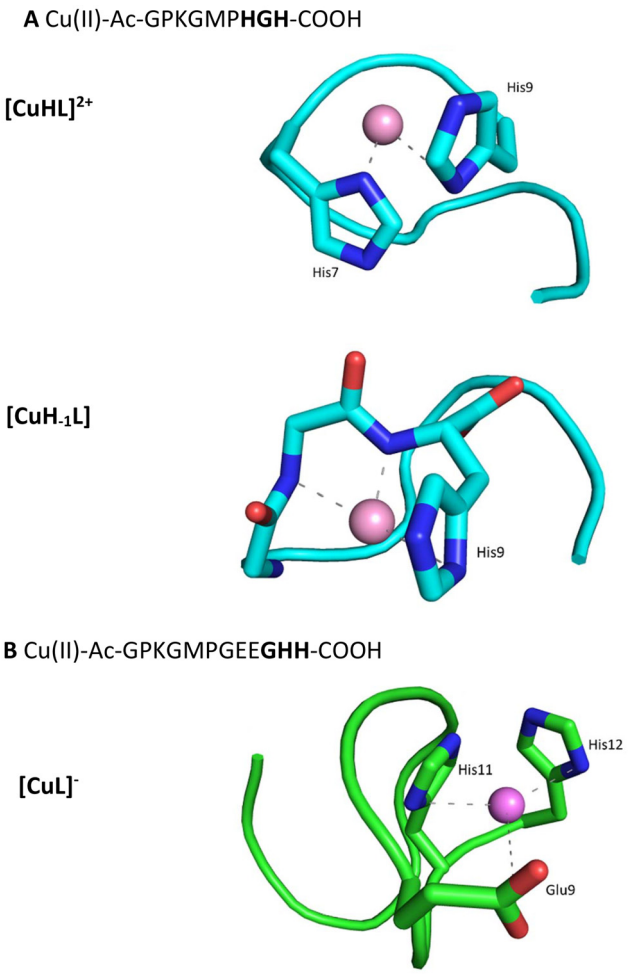


**Fig. 6** Schematic coordination models corresponding to the dominant Cu(II) complex species present at pH 7.4 for (A) Ac-GPKGMP**HGH**-COOH and (B) Ac-GPKGMPGEE**GHH**-COOH, as identified by potentiometric speciation and supported by UV–Vis, CD, EPR and NMR data.

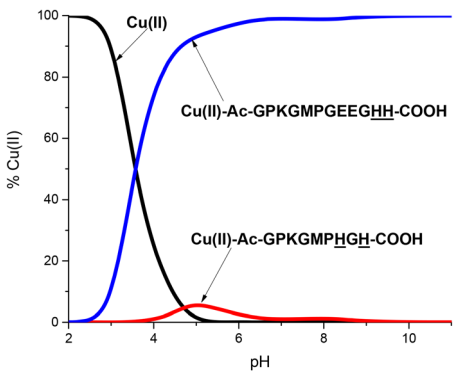


**Fig. 7** Competition plots for a simulated solution containing equimolar concentrations of Cu(II), Ac-GPKGMP**HGH**-COOH and Ac-GPKGMPGEE**GHH**-COOH. The diagram is calculated from the overall stability constants of the binary complexes and simulate a situation in which equimolar concentrations of all of the chosen ligands and metal are present in a solution.

lack of an amide group in proline removes one potential backbone donor and restricts binding registers that rely on amide deprotonation, while its conformational rigidity may disfavor geometries optimal for amide-rich Cu(II) coordination. This effect is secondary to, but consistent with, the lower thermodynamic stability of the Cu(II)-HGH complex.

### Potentiometric and spectroscopic studies of Zn(II) complexes

While the biological role of CopT is strictly associated with copper sensing, the use of Zn(II) in coordination studies of histidine-containing motifs is a well-established strategy to probe their intrinsic metal-binding properties in the absence of redox chemistry. Unlike Cu(II), Zn(II) is spectroscopically silent, redox-inactive, and does not promote amide deprotonation, allowing the coordination preferences of imidazole and carboxylate donor groups to be examined.

In the Zn(II)–Ac-GPKGMP**HGH**-COOH system, $[ZnHL]^{2+}$ is the first complex species to reach its maximum concentration at pH 7, with two histidine residues already deprotonated and coordinating the Zn(II) ion. The appearance of the $[ZnH_{-1}L]$ species results from the subsequent deprotonation of two water molecules, which bind to Zn(II) and lead to the formation of a $2N_{im}$, $2OH^-$ complex. The last calculated species, $[ZnH_{-2}L]^-$, characterized by a p$K_a$ value of 10.05, indicates the involvement of a third water molecule in Zn(II) binding. Zn(II) may adopt a five-coordinate, trigonal bipyramidal geometry involving a $2N_{im}$, $3OH^-$ donor set. Alternatively, the additional hydroxide ligand may replace one histidine donor, preserving a four-coordinate environment with a $1N_{im}$, $3OH^-$ coordination mode (Table 3(A) and Fig. 8A).

**Table 3** Stability constants (log $\beta$) for (A) Zn(II)–Ac-GPKGMP**HGH**-COOH and (B) Zn(II)–Ac-GPKGMPGEE**GHH**-COOH complexes in aqueous solution of 4 mM $HClO_4$ with $I$ = 0.1 M $NaClO_4$ at 25 °C. M : L molar ratio = 0.9 : 1

| Species | log $\beta$ | p$K_a$ |
|---|---|---|
| (A) Zn(II)–Ac-GPKGMP**HGH**-COOH | | |
| $[ZnHL]^{2+}$ | 14.77(4) | |
| $[ZnH_{-1}L]$ | −1.68(5) | |
| $[ZnH_{-2}L]^-$ | −11.73(6) | 10.05 |
| (B) Zn(II)–Ac-GPKGMPGEE**GHH**-COOH | | |
| $[ZnH_3L]^{2+}$ | 29.14(1) | |
| $[ZnH_2L]^+$ | 24.54(1) | 4.60 |
| ZnHL | 18.09(2) | 6.45 |
| $[ZnL]^-$ | 11.25(2) | 6.84 |
| $[ZnH_{-1}L]^{2-}$ | 3.42(4) | 7.83 |

At pH 7.4, the NMR spectra confirm the coordination of the Zn(II) ion by two histidyl residues. The addition of Zn(II) induced a disappearance of both the amide and aromatic correlations for His7 and His9 (Fig. 9A), as well as their aliphatic correlations (Fig. 9B). Although Gly1, Gly4, and Gly8 could not be individually assigned, a total broadening of one of the three NH-Hα correlation peaks was observed (Fig. 9A); this effect is likely attributable to Gly8, given its sequence position between the two primary anchoring sites, His7 and His9. Methionine 5 exhibited a complex set of perturbations upon Zinc addition: while the NH-Hα correlation remained unchanged, the NH-Hγ signal underwent total broadening, and the NH-Hβ correlation showed a significant downfield shift of 0.03 ppm (Fig. 9A). A similar effect was observed for the Hγ–Hβ correlation, which exhibited a downfield shift of 0.02 ppm (Fig. 9B). Moreover, also the signal of the S–$CH_3$ group is slightly shifted and extensively broadened upon metal addition (Fig. 9C). Finally, Pro6 correlations involving the Hβ protons, as well as one of the two Hγ protons, underwent total broadening, while the second Hγ proton displayed a notable downfield shift of 0.03 ppm. Experimental evidence at pH 7.4 suggests that the Zn(II) ion is coordinated to the imidazole nitrogens of His7 and His9, with the thioether group of Met5 completing the metal's coordination sphere.

For the second ligand, Ac-GPKGMPGEE**GHH**-COOH, $[ZnH_3L]^{2+}$, likely involves zinc binding to the carboxyl groups of glutamic acid residues. The appearance of the next two species, $[ZnH_2L]^+$ and [ZnHL], with significantly shifted p$K_a$ values (4.60 and 6.45 compared to 6.75 and 7.53 for the free ligand), indicates the involvement of both histidine side chains in Zn(II) coordination. The next two species, $[ZnL]^-$ and $[ZnH_{-1}L]^{2-}$, with p$K_a$ values of 6.84 and 7.83, confirm the par-

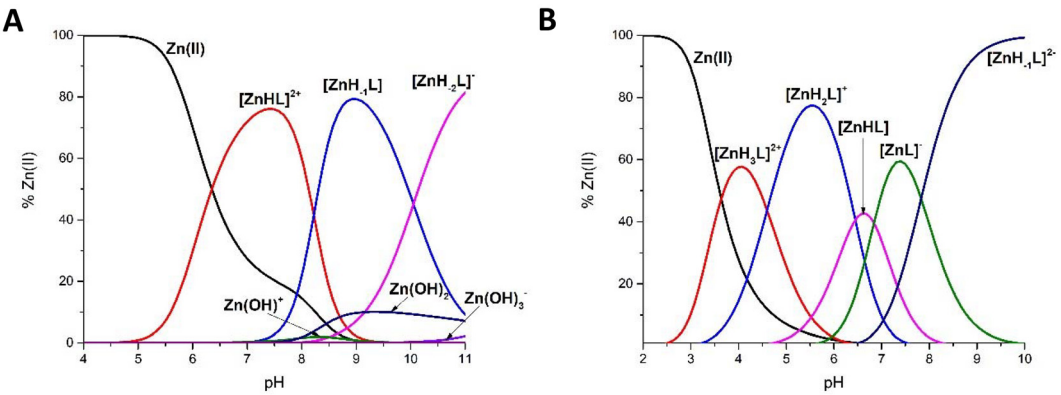


**Fig. 8** Distribution diagrams for the formation of Zn(II) complex with (A) Ac-GPKGMP**HGH**-COOH and (B) Ac-GPKGMPGEE**GHH**-COOH, $T$ = 298 K and $I$ = 0.1 M ($NaClO_4$), M : L molar ratio = 0.9 : 1.

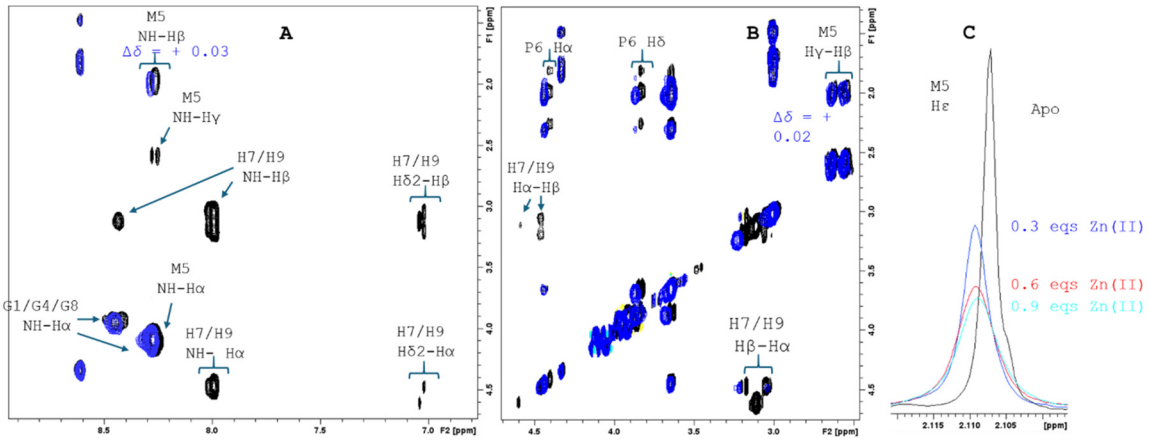


**Fig. 9** Superimposition of the amide and aromatic (A) and aliphatic (B) regions of 2D $^{1}H-^{1}H$ TOCSY spectra of Ac-GPKGMPHGH-COOH recorded in absence (black) and in presence of 0.9 Zn(II) eq. (blue). (C) The superimposition of the Met5 methyl peak in 1D spectra during the Zn(II) titration. $T$ = 288 K, $C_M$ = 0.5 mM, phosphate buffer = 20 mM, pH 7.4.

ticipation of water molecules in Zn(II) binding, leading to the formation of a $2N_{im}$, $2OH^-$ donor set (Table 3(B) and Fig. 8B).

To examine the involvement of individual donor groups suggested by potentiometric analysis, NMR experiments were carried out at pH 7.4. At this pH, speciation calculations indicate the coexistence of three complex species, ZnHL, ZnL, and $ZnH_{-1}L$, each differing in protonation state and donor set. Upon addition of 0.9 equivalents of Zn(II), His11 and His12 exhibited only marginal chemical shift perturbations, with no detectable line broadening in either 1D or 2D spectra. Only a very small downfield shift (~0.01 ppm) was observed for the NH-Hβ correlations of both histidines (Fig. S3), while signals associated with glutamic acid residues remained unchanged. The absence of significant chemical shift changes or resonance broadening might be dependent on a fast exchange regime on the NMR timescale, in which observed resonances represent population-weighted averages over multiple interconverting coordination states. Given the $d^{10}$ electronic configuration and high kinetic lability of Zn(II), together with the simultaneous presence of three different complex species involving alternative combinations of imidazole, carboxylate, and hydroxide/water donors, rapid interconversion between distinct coordination geometries is expected. Such dynamic speciation results in extensive averaging of local electronic environments, resulting in only weak observable NMR perturbations despite thermodynamically significant Zn(II) binding. Consequently, Zn(II) coordination to the GHH-containing peptide at pH 7.4 is best described as strong yet structurally heterogeneous and dynamically averaged in solution, reconciling the potentiometric and NMR observations.

The competition plot for Zn(II) and **HGH** and **GHH** sequences (Fig. S4) shows a behavior remarkably similar to that observed for Cu(II) (Fig. 7). The **GHH**-containing sequence becomes the dominant Zn(II) binder upon increasing pH, whereas the **HGH** motif contributes only marginally to metal binding across the studied pH range.

This similarity is particularly informative because, in contrast to Cu(II), Zn(II) does not readily involve deprotonated amide nitrogens in its coordination sphere and typically prefers neutral imidazole and carboxylate donors. Therefore, the analogous outcome of the competition simulation for both metal ions indicates that the decisive factor governing metal preference is not the specific coordination chemistry of Cu(II), but rather intrinsic differences in the ligand donor sets. In this context, the presence of two glutamate residues in the **GHH** sequence plays a central role. Carboxylate side chains provide efficient anchoring sites for Zn(II) already at acidic pH, facilitating early complex formation before histidine imidazole groups become fully available for coordination. In contrast, the HGH motif lacks such acidic donors and relies primarily on histidine coordination, which delays effective Zn(II) binding under comparable conditions. The fact that both Cu(II) and Zn(II) exhibit the same competition behavior strongly supports the conclusion that the observed preference originates primarily from the presence of the EE fragment and the resulting carboxylate-assisted binding pathway, rather than from differences in histidine spacing or metal-specific coordination modes, which may contribute to the thermodynamic favoring of binding of adjacent amide nitrogens at higher pH.

Zn(II) binding to the HGH- and GHH-containing peptides at pH 7.4 is characterized by the coexistence of multiple coordination states (especially for GHH motif) and rapid interconversion between alternative donor environments. Under these conditions, Zn(II) coordination remains dominated by side-chain donors and does not promote persistent involvement of the peptide backbone. The following schematic representations (Fig. 10) therefore provide a conceptual summary of the Zn(II) binding environments sampled by the two motifs under physiological conditions.

### The influence of Cu(II) and Zn(II) ions on the structure of Ac-GPKGMPHGH-COOH and Ac-GPKGMPGEEGHH-COOH

To assess whether metal coordination is accompanied by changes in the backbone organization of these intrinsically disordered CopT C-terminal fragments, far-UV CD spectra were

 

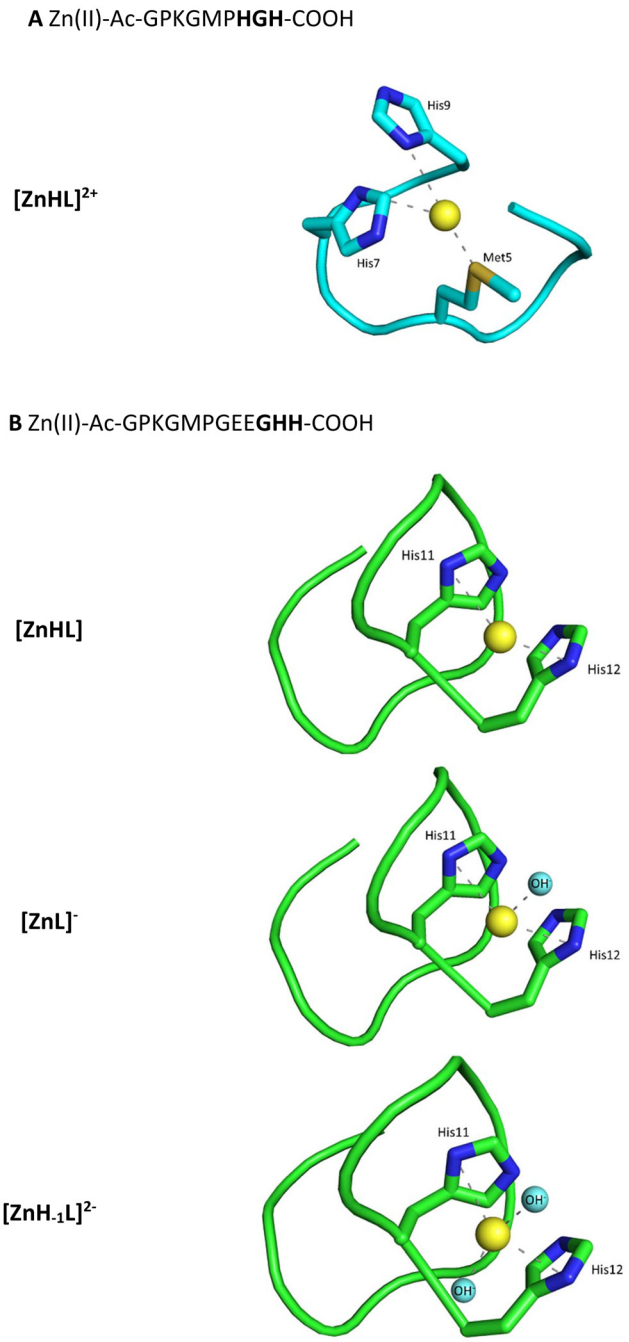


**Fig. 10** Schematic coordination models corresponding to the dominant Zn(II) complex species present at pH 7.4 for (A) Ac-GPKGMP**HGH**-COOH and (B) Ac-GPKGMPGEE**GHH**-COOH, as identified by potentiometric speciation and supported by NMR data.

recorded across the entire pH range for the apo peptides and their Cu(II) and Zn(II) complexes (Fig. S5 and S6). The far-UV CD spectra of both peptides in their apo forms (Fig. S5A and S6A) show a characteristic minimum at 198 nm across the entire pH range, consistent with predominantly disordered, random-coil conformations typical for short, flexible sequences. A very similar behaviour is observed for the Zn(II) complexes (Fig. S5C and S6C). The overall shape of the spectra remains close to that of the apo peptides, indicating that zinc coordination through imidazole and carboxylate donors does not significantly affect the backbone organization. In contrast, clear spectral changes appear in the presence of Cu(II) (Fig. S5B and S6B). With increasing pH, the characteristic random-coil minimum becomes progressively less pronounced and a distinct negative band develops in the 220–240 nm region. These changes correlate directly with the formation of Cu(II) species involving deprotonated amide nitrogen donors, demonstrating that copper coordination induces a measurable reorganization of the peptide backbone. This effect is particularly evident in the direct comparison at pH 7.5 (Fig. S5D and S6D). While both apo and Zn(II) forms retain a random-coil-like profile, the Cu(II) complexes display a distinctly altered spectral shape, indicating a transition toward a more conformationally restricted, helix-like arrangement of the backbone rather than formation of a classical α-helix. Notably, this Cu(II)-induced change is more pronounced for the **HGH** peptide (Fig. S5B) than for the **GHH** sequence (Fig. S6B). This difference is consistent with the speciation data: at pH 7.5 the HGH system is already significantly shifted toward amide-involving coordination modes, whereas in the GHH peptide a substantial fraction of imidazole-dominated species is still present, and the amide-rich coordination becomes dominant only at slightly higher pH. At pH approximately 11, another distinct transformation of the Cu(II) spectra is observed for both peptides, characterized by the appearance of a positive band near 215 nm (Fig. S5B and S6B). In this pH region, the dominant species corresponds to the $1N_{im}$, $3N^{-}$ coordination mode. Chelation by three successive deprotonated amide nitrogens imposes a highly ordered, nearly planar arrangement of peptide bonds, which strongly restricts backbone flexibility. The resulting CD feature does not indicate β-sheet formation but rather reflects the enforced geometry of the peptide backbone dictated by the amide-rich copper chelate.

## Conclusions

In this work, we provide a bioinorganic insight into Cu(II) and Zn(II) coordination by histidine-containing C-terminal motifs derived from archaeal CopT regulators, using the minimal peptide models Ac-GPKGMP**HGH**-COOH and Ac-GPKGMPGEE**GHH**-COOH. A combined potentiometric, spectroscopic and NMR approach demonstrates that both sequences form exclusively mononuclear complexes with Cu(II) and Zn(II), with well-defined and pH-dependent coordination modes.

At pH 7.4 Cu(II) binding in both peptides is dominated by histidine imidazole coordination. For the HGH-containing sequence, the prevalent Cu(II) species is characterized by a $2N_{im}$ and $1N_{im}$, $2N^{-}$ donor set. In the GHH-derived peptide, Cu(II) is likewise coordinated by two histidine imidazole nitrogens, but the presence of adjacent glutamate residues provides additional electrostatic stabilization, resulting in significantly

higher overall complex stability while preserving the same primary donor set. NMR spectroscopy confirms direct involvement of the histidine residues in both systems and identifies proximal residues contributing to the local metal-binding environment.

For Zn(II), coordination at pH around 7–7.5 is dominated by histidine imidazole binding in both peptides. In the HGH peptide, Zn(II) is coordinated predominantly by two histidine imidazole nitrogens, with NMR data indicating weak, secondary involvement of the methionine thioether and water molecule in completing the coordination sphere. In the GHH-derived peptide, Zn(II) binding at neutral pH is best described as a dynamic mixture of coexisting species, in which two histidine residues are the only donors that can be unambiguously identified experimentally, while the remaining aspects of the coordination environment are averaged by rapid interconversion on the NMR timescale.

Comparison of the two C-terminal motifs demonstrates that the markedly higher affinity of the GHH sequence for both Cu(II) and Zn(II) originates from its carboxylate-assisted binding environment, rather than from differences in histidine spacing or primary coordination mode. Thus, at physiologically relevant pH, both motifs employ the same histidine-based Cu(II) and Zn(II) anchoring strategy, while secondary donor groups modulate stability and dynamics.

Far-UV CD measurements further show that Cu(II), but not Zn(II), induces pronounced conformational restriction of the peptide backbone upon formation of amide-rich coordination modes, highlighting a unique ability of Cu(II) to couple metal binding with structural reorganization of intrinsically disordered CopT terminal fragments. This effect is especially relevant in the context of metalloregulation, where metal-induced conformational changes may contribute to signal transduction rather than simple metal sequestration.

These findings demonstrate how subtle variations in short peptide sequences encode fundamentally different metal-binding pathways and thermodynamic preferences. Histidine and carboxylate-rich motifs emerge as chemically autonomous metal-binding elements that can operate independently of canonical cysteine-based domains. Together, the results extend the current cysteine-centered view of CopT regulators and suggest that multiple, chemically orthogonal Cu(II)-binding environments may coexist within the CopT C-terminal region.

The identification of conserved histidine-containing motifs in the C-terminal regions of CopT homologues, together with their demonstrated ability to form stable Cu(II) complexes, suggests that these sequences are not random but may have a functional role in metal binding. Given the flexible nature of C-terminal segments, they may act as adaptable elements capable of capturing copper ions and contributing to metal recognition or buffering. Flexible, histidine-rich regions have been previously implicated in transient metal binding and metal buffering in metalloproteins.[24,26,52]

Taken together, these results support a model in which the intrinsically disordered C-terminal region of CopT is not merely a passive extension, but a chemically active element that contributes to metal binding through sequence-encoded, adaptable coordination motifs.

## Author contributions

Wojciech Lizak: investigation (potentiometry, UV-Vis, CD, MS), visualization, writing – review & editing. Klaudia Kłoptowska: investigation (potentiometry, UV-Vis, CD, EPR), visualization. Arian Kola: investigation (NMR), formal analysis, validation, writing – review & editing, visualization. Daniela Valensin: investigation (NMR), formal analysis, validation, writing – review & editing. Aleksandra Hecel: conceptualization, formal analysis, methodology, writing – original draft, writing – review & editing, supervision, funding acquisition, project administration, validation.

## Conflicts of interest

The authors declare no conflict of interest.

## Data availability

The datasets generated and analysed during the current study are available from the corresponding author on reasonable request.

Supplementary information (SI) is available. See DOI: https://doi.org/10.1039/d6dt00501b.

## Acknowledgements

This work was supported by the National Science Centre, Poland (grant no. UMO-2023/51/D/ST5/01798).

## References

1 D. Capdevila, K. Edmonds and D. Giedroc, *Bioinorg. Chem.*, 2017, **61**, 177–200.
2 Z. Chen, Y. Fu, J. Li, J. Wang and X. Fang, *iScience*, 2025, **28**, 114084.
3 A. Andrei, Y. Öztürk, B. Khalfaoui-Hassani, J. Rauch, D. Marckmann, P. Trasnea, F. Daldal and H. Koch, *Membranes*, 2020, **10**, 242.
4 L. Novoa-Aponte and J. Argüello, *J. Biol. Inorg. Chem.*, 2022, **27**, 509–528.
5 D. Capdevila, J. Rondón, K. Edmonds, J. Rocchio, M. Dujovne and D. Giedroc, *Chem. Rev.*, 2024, **124**, 13574–13659.
6 Z. Ma, F. Jacobsen and D. Giedroc, *Chem. Rev.*, 2009, **109**, 4644–4681.

 

7 N. Hirth, M. Gerlach, N. Wiesemann, M. Herzberg, C. Grosse and D. Nies, *Appl. Environ. Microbiol.*, 2023, **89**, e00567-23.
8 L. Busenlehner, M. Pennella and D. Giedroc, *FEMS Microbiol. Rev.*, 2003, **27**, 131–143.
9 P. Gautam, I. Erill and K. Cusick, *Microorganisms*, 2023, **11**, 1012.
10 D. Osman and J. Cavet, *Nat. Prod. Rep.*, 2010, **27**, 668–680.
11 K. Higgins, H. Hu, P. Chivers and M. Maroney, *Biochemistry*, 2013, **52**, 84–97.
12 T. Ettema, A. Brinkman, P. Lamers, N. Kornet, W. de Vos and J. van der Oost, *Microbiology*, 2006, **152**, 1969–1979.
13 C. Martínez-Bussenius, C. Navarro and C. Jerez, *Microb. Biotechnol.*, 2017, **10**, 279–295.
14 A. Villafane, Y. Voskoboynik, M. Cuebas, I. Ruhl and E. Bini, *Biochem. Biophys. Res. Commun.*, 2009, **385**, 67–71.
15 C. Völlmecke, S. Drees, J. Reimann, S. Albers and M. Lübben, *Microbiology*, 2012, **158**, 1622–1633.
16 T. Ettema, M. Huynen, W. de Vos and J. van der Oost, *Trends Biochem. Sci.*, 2003, **28**, 170–173.
17 F. Grunberger, R. Reichelt, I. Waege, V. Ned, K. Bronner, M. Kaljanac, N. Weber, Z. El Ahmad, L. Knauss, M. Madej, C. Ziegler, D. Grohmann and W. Hausner, *Front. Microbiol.*, 2021, **11**, 613532.
18 J. U. Linder, *PLoS One*, 2015, **10**, e0141843.
19 E. Bini, *FEMS Microbiol. Ecol.*, 2010, **73**, 1–16.
20 S. Kim, H. Jeong, M. Kim, A. Choi, M. Kim, S. Kang and S. Lee, *BioMetals*, 2019, **32**, 923–937.
21 T. Rae, P. Schmidt, R. Pufahl, V. Culotta and T. O'Halloran, *Science*, 1999, **284**, 805–808.
22 J. Olson and C. Kellogg, *FEMS Microbiol. Ecol.*, 2010, **73**, 17–30.
23 C. Baker-Austin, M. Dopson, M. Wexler, R. Sawers and P. Bond, *Microbiology*, 2005, **151**, 2637–2646.
24 K. Waldron and N. Robinson, *Nat. Rev. Microbiol.*, 2009, **7**, 25–35.
25 A. Monteith and E. Skaar, *Trends Endocrinol. Metab.*, 2021, **32**, 916–928.
26 N. J. Robinson and D. R. Winge, in *Annual Review of Biochemistry*, ed. R. D. Kornberg, C. R. H. Raetz, J. E. Rothman and J. W. Thorner, Annual Reviews, Palo Alto, 2010, vol. 79, pp. 537–562.
27 G. Gran, *Acta Chem. Scand.*, 1950, **4**, 559–577.
28 P. Gans and B. O'Sullivan, *Talanta*, 2000, **51**, 33–37.
29 P. Gans, A. Sabatini and A. Vacca, *J. Chem. Soc., Dalton Trans.*, 1985, 1195–1200.
30 P. Gans, A. Sabatini and A. Vacca, *Talanta*, 1996, **43**, 1739–1753.
31 L. Alderighi, P. Gans, A. Ienco, D. Peters, A. Sabatini and A. Vacca, *Coord. Chem. Rev.*, 1999, **184**, 311–318.
32 N. Y. C. F. Baes and R. S. Mesmer, *The Hydrolysis of Cations*, John Wiley & Sons, London, Sydney, Toronto, 1976.
33 T. L. Hwang and A. J. Shaka, *J. Magn. Reson., Ser. A*, 1995, **112**, 275–279.
34 G. Grimsley, J. Scholtz and C. Pace, *Protein Sci.*, 2009, **18**, 247–251.
35 I. Sovago and K. Osz, *Dalton Trans.*, 2006, 3841–3854.
36 H. M. Irving, M. G. Miles and L. D. Pettit, *Anal. Chim. Acta*, 1967, **38**, 475–488.
37 B. Bjellqvist, G. Hughes, C. Pasquali, N. Paquet, F. Ravier, J. Sanchez, S. Frutiger and D. Hochstrasser, *Electrophoresis*, 1993, **14**, 1023–1031.
38 A. Hecel, A. Kola, D. Valensin and D. Witkowska, *Inorg. Chem.*, 2025, **64**, 2936–2950.
39 D. Kyriakou, E. Bletsa, V. Moussis, Y. Deligiannakis and G. Malandrinos, *Dalton Trans.*, 2022, **52**, 58–69.
40 H. Sigel and R. B. Martin, *Chem. Rev.*, 1982, **82**, 385–426.
41 N. Jakab, A. Jancsó, T. Gajda, B. Gyurcsik and A. Rockenbauer, *J. Inorg. Biochem.*, 2008, **102**, 1438–1448.
42 J. Kaminska, A. Hecel, J. Slowik, A. Rombel-Bryzek, M. Rowinska-Zyrek and D. Witkowska, *Front. Mol. Biosci.*, 2024, **11**, 1366588.
43 D. Dudek, A. Miller, A. Hecel, A. Kola, D. Valensin, A. Mikolajczyk, M. Barcelo-Oliver, A. Matera-Witkiewicz and M. Rowinnska-Zyrek, *Inorg. Chem.*, 2023, **62**, 14103–14115.
44 A. Myari, G. Malandrinos, J. Plakatouras, N. Hadjiliadis and I. Sovago, *Bioinorg. Chem. Appl.*, 2003, 99–112.
45 D. Bellotti, S. Leveraro, A. Hecel and M. Remelli, *Anal. Biochem.*, 2023, **680**, 115315.
46 B. Balogh, Z. Bihari, P. Buglyó, G. Csire, Z. Kerekes, M. Lukács, I. Sóvágó and K. Várnagy, *New J. Chem.*, 2019, **43**, 907–916.
47 A. Hecel, K. Garstka, H. Kozloeski and M. Rowinska-Zyrek, *J. Inorg. Biochem.*, 2024, **252**, 112456.
48 E. Szekely, G. Csire, B. Balogh, J. Erdei, J. Király, J. Kocsi, J. Pinkóczy and K. Várnagy, *Molecules*, 2022, **27**, 3435.
49 H. Kozlowski, W. Bal, M. Dyba and T. Kowalik-Jankowska, *Coord. Chem. Rev.*, 1999, **184**, 319–346.
50 D. Bellotti, D. Loboda, M. Rowinska-Zyrek and M. Remelli, *New J. Chem.*, 2018, **42**, 8123–8130.
51 J. Watly, A. Hecel, M. Rowinska-Zyrek and H. Kozlowski, *Inorg. Chim. Acta*, 2018, **472**, 119–126.
52 S. Tottey, K. Waldron, S. Firbank, B. Reale, C. Bessant, K. Sato, T. Cheek, J. Gray, M. Banfield, C. Dennison and N. Robinson, *Nature*, 2008, **455**, 1138–U1117.